Diffusion of active particles in a complex environment: role of surface scattering

Theresa Jakuszeit,* Ottavio A. Croze, and Samuel Bell†
Cavendish Laboratory, University of Cambridge, Cambridge CB3 0HE, U.K.
(Dated: January 13, 2019)

Experiments have shown that self-propelled particles can slide along the surface of a circular obstacle without becoming trapped over long times. Using simulations and theory, we study the impact of boundary conditions on the diffusive transport of active particles in an obstacle lattice. We find that particle dynamics with sliding boundary conditions result in large diffusivities even at high obstacle density, unlike classical specular reflection. These dynamics are very well described by a model based on Run-and-Tumble particles with microscopically derived reorientation functions arising from obstacle-induced tumbles. This model, however, fails to describe fine structure in the diffusivity at high obstacle density predicted by simulations for pusher-like collisions. Using a simple deterministic model, we show that this structure results from particles being guided by the lattice. Our results thus show how non-classical surface scattering introduces a dependence on the lattice geometry at high densities. We discuss implications for the study of bacteria in complex environments.

I. INTRODUCTION

The field of active matter covers the broad spectrum of particles which move by consuming energy from their environment [1]. These range from flocks of birds and insect swarms [2, 3], to cell tissues [4], microswimmers [5], microtubuli [6, 7], and enzymes [8]. Microswimmers such as bacteria and Janus particles self-propel at low Reynolds numbers, the latter being directly powered by an asymmetric chemical reaction on the particle surface, the former by rotating helical filaments. The propulsive mechanisms set up complicated hydrodynamic flows, which determine the characteristics of interactions, both with other microswimmers, and with the boundaries of their environment. These boundary interactions may perform an essential function in nature. Surface-induced accumulation is an important step in the formation of biofilms, which are involved in many chronic diseases and pathogen spread [9, 10]. Blood pathogens are adapted to swimming in crowded environments [11], sperm cells follow the wall of the genital tract to reach the egg cell [12–14], and artificial Janus particles have been guided along microfluidic edges [15] and through obstacle arrays [16–18].

The nature of particle-surface interactions relies on a microswimmer's propulsion mechanism, including steric and hydrodynamic effects. Microalgae, which are "puller" type swimmers, are scattered off surfaces [19–21], leading to billiard-like motion in polygon structures [22]. In contrast, "pusher" type swimmers, such as bacteria or Janus particles, are trapped by hydrodynamic effects near flat surfaces, where they accumulate [23–25]. When the surface is instead convex, this trapping time can be reduced [26]. In particular, bacteria trace along convex surfaces such as microfluidic pillars before escaping with a small angle [27].

* tj295@cam.ac.uk
† sb855@cam.ac.uk

The modelling of these scenarios typically follows one of two approaches: hydrodynamic models, or random walk models. With a full hydrodynamic approach, the particle-surface interactions can be studied by modelling the active particle as a hard sphere with defined tangential surface velocity [28]. A recent study explored the migration of active particles through a body-centered cubic lattice of spheres of the same size as the particle [29]. Depending on the swimmer type and packing density, the authors found trapped, random walk and straight trajectories. The computational demands of the simulations, however, prevented study of long-time behavior. Random walk models can be used to study the diffusive behavior of active particles. Diffusion in complex media has been studied for several boundary interactions: for model particles that evade obstacles [30], particles that are trapped before being randomly reorientated [31], and particles that interact with obstacles via an excluded volume potential [32]. Hydrodynamic boundary interactions have been shown to play an important role in active systems, e.g. in the control of flow-induced phase separation [33]. Similarly, pusher-type boundary interactions may guide microswimmers through their environment [15, 34], which would facilitate diffusion.

In this paper, we study theoretically how these different modes of boundary scattering influence the diffusive transport of active particles in ordered arrays of obstacles. We consider particles specularly reflected from boundaries, as in the Lorentz gas model [35]; particles that scatter by sliding around obstacles, like pushers [26, 27]; and particles that interact with obstacles via a steric, torque-free interaction, which we refer to here as a "slide-off" condition [32]. For these 'pusher-like' collisions, our simulations and a run-and-tumble particle model predict, counterintuitively, that large diffusive transport is possible even at high obstacle densities. This result contrasts sharply with the expected low diffusivity of Lorentz gas particles at high densities. We show for the sliding condition, using a simple deterministic model, how this large diffusion at high density is caused by par-

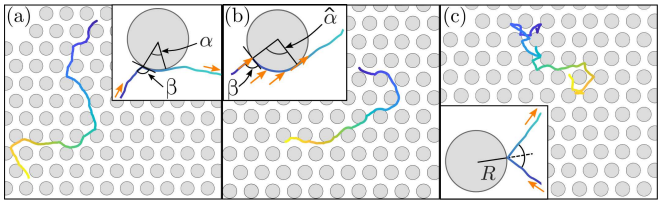

FIG. 1. Boundary conditions. Typical trajectory of a particle governed by Eqs. (1) and (2) with (a) a sliding, (b) a slide-off, or (c) a reflecting boundary condition. For the sliding condition, particle leaves at a tangent to the obstacle after traversing a fixed central angle α. For the slide-off condition, the central angle $\hat{\alpha}$ depends on the incident angle, the obstacle radius, and the magnitude of rotational diffusion on the obstacle.

ticle guiding by the lattice. Simulations show that the same effect occurs for the slide-off condition, but not for Lorentz gases. Our results highlight the previously unexplored role of lattice geometry in active particle transport.

II. MODEL

We consider N_P active particles in a two-dimensional space in which obstacles are placed in a hexagonal lattice. The centers of the obstacles are fixed with distance d, and the obstacle radius R is varied. The equations of motion for the i-th particle are given by

$$\dot{\mathbf{x}}_i = v\,\mathbf{p}(\varphi_i) \tag{1}$$

$$\dot{\varphi}_i = \sqrt{2D_R}\xi_i(t), \tag{2}$$

where dot denotes the time derivative, v is the particle speed, $\mathbf{x}_i$ and φ_i correspond to the position and moving direction of the i-th particle, respectively, and the unit vector $\mathbf{p} = [\cos\varphi, \sin\varphi]$. The white noise in Eq. (2) obeys $\langle\xi(t)\rangle = 0$ and $\langle\xi_i(t)\xi_j(t')\rangle = \delta_{ij}\delta(t-t')$. Thus, the moving direction undergoes rotational diffusion with $\langle\varphi(t)^2\rangle = 2D_R t$. As a result, the particle performs a persistent random walk with persistence length $l_p = v/D_R$ [36].

Recent microfluidic experiments [26] and hydrodynamic models [26, 27] have shown that pillars with radii above a critical threshold strongly trap pushers, which escape at long times by rotational diffusion. We consider in this study only pillars with radii below this critical threshold (and so choose parameters motivated by experiment [34, 37]). In this case, swimmers collide with an obstacle at an angle β, defined as the angle between the tangent at the collision point and the orientation $\mathbf{p}$. If $\beta < \pi/2$, the particle travels clockwise around the obstacle; if $\beta \geq \pi/2$, the particle travels counter-clockwise. After the collision, the angle between it and the obstacle surface tangent decreases until escape [27].

To capture the non-classical particle-surface interaction, we introduce a sliding boundary condition [26]. Consider a collision with an obstacle: β is defined as the angle between the tangent at the collision point and the orientation $\mathbf{p}$. The particle moves along the obstacle to traverse a central angle α (Fig. 1(a) inset). A model of stochastic dynamics could determine, for a given incident β, the resulting distribution of central angles α (leaving times). However, such a model has yet to be developed. We know from modelling and experiments that after collision, the particle quickly rotates, through phoretic and/or hydrodynamic interactions with the surface, to align its orientation vector with the surface, regardless of the orientation of the particle upon collision [10, 38]. This rotation generally occurs on a much faster timescale than the trapping time of the particle. Therefore, we choose to neglect the dependence of the sliding angle α on β, i.e., model the probability distribution of α as $P(\alpha)$ instead of as $P(\alpha|\beta)$, with $P(\alpha)$ peaked at some value $\alpha^{\max}$ determined by the competition between rotational diffusion and deterministic alignment with the surface. In this work we explore the effect of boundary conditions assuming a fixed central angle α and further assume that, when a particle leaves an obstacle, its orientation $\mathbf{p}$ is tangent to the obstacle surface. This is a necessary simplification of the hydrodynamic behaviour of pusher-type particles at convex obstacles. Our model also neglects any potential impact of the chemical field surrounding synthetic active particles. The neglect of stochasticity in α can be checked by simulations. Results (not shown) with a fixed (mean) α are qualitatively the same to those obtained with a distribution of α, provided the latter is peaked about its mean (e.g. a Gamma distribution).

As a comparison, we also consider a slide-off boundary condition, and a reflecting boundary condition. In the slide-off condition, when a particle collides with an obstacle, it retains its orientation vector, and advances around the obstacle depending on the component of its velocity parallel to the obstacle surface (initially β) , i.e. $v = v_0\cos\beta$, as shown in Fig. 1(b). The angle between particle orientation and obstacle tangent decreases as the particle moves around the obstacle's surface. It will leave the obstacle when the orientation vector is parallel to (or pointing away from) the obstacle's surface. In the absence of rotational diffusion, this means that the particle will traverse a central angle of $\hat{\alpha} = \min(\beta, \pi - \beta)$, and so it bears some resemblance to the sliding condition. However, while sliding is motivated by hydrodynamic effects, the slide-off condition is motivated by steric effects, and has been used in various potential-based simulation studies to model Janus particles and active disks [32, 39].

For the reflecting condition, a particle is reflected with an angle equal to the incident angle, as illustrated in Fig. 1(c). This interaction type implies time-reversibility, which is an assumption underlying gas kinetic models derived for bacteria transport in porous media [40, 41]. By contrast, both the sliding and slide-off boundary condition are not time-reversible and violate detailed balance [5]. The system of Eqs. (1) and (2) is solved numerically, and example particle tracks are shown in Fig. 1.

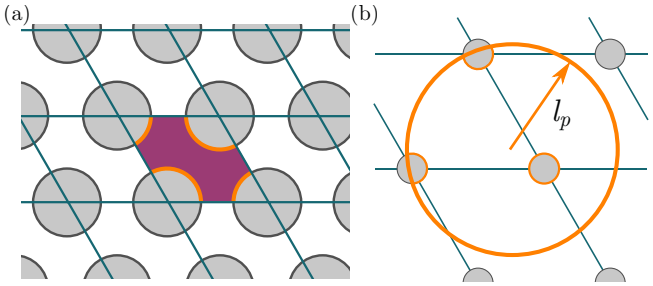

FIG. 2. An illustration of the lattice geometry in the reflecting boundary condition calculation. A hexagonal lattice can be patterned by rhombi of side length equation to the lattice spacing, as shown in (a). The shaded area is the area available to particles per unit cell, A, while the orange arcs highlight the obstacle surface per unit cell $P = 2\pi R$. In (b), an extra circular boundary is added, with a radius of the persistence length, to account for reorientation via rotational diffusion, and preventing an infinite mean free path at low densities.

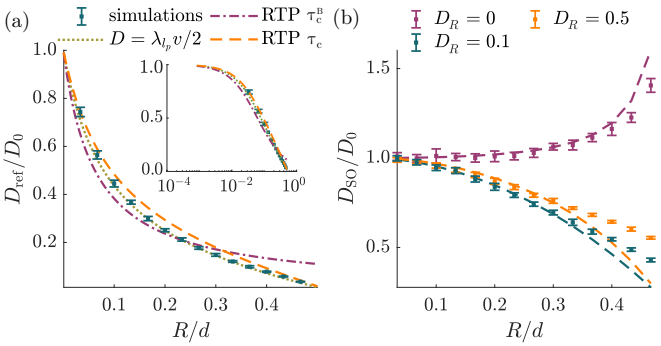

FIG. 3. Diffusion with reflecting and slide-off boundary condition. (a) Diffusion with reflecting boundary condition, $D_{\rm ref}$, is scaled by diffusion coefficient in the absence of any obstacles, $D_0 = v^2/2D_R$. Simulations agree with Santalo's formula that was adjusted for rotational diffusion, λ_{l_P} (green dotted curve). The run-and-tumble model in Eq. (3) with Santalo mean free path λ in $\tau_c = \lambda/v$ (orange dashed) is compared to RTP model with $\tau_c^B = 1/\rho$ [31] (purple dashed-dotted) and $\langle \cos\psi \rangle = -1/3$. (b) Diffusion with slide-off boundary condition, $D_{\rm SO}$, is scaled by the free diffusion coefficient. If the particle orientation is fixed on the obstacle (i.e. $D_R = 0$ on obstacle), diffusion is enhanced at large obstacle densities (purple markers). With stochastic slide-off boundary condition (i.e. $D_R \neq 0$), the diffusion coefficient decreases with increasing obstacle density. If D_R is increased (both free space and on obstacle), the relative decrease in diffusion coefficient, $D_{\rm SO}/D_0$, due to obstacle collisions is smaller (orange vs. green markers). Note that absolute value of $D_{\rm SO}$ is smaller for larger D_R. The dashed lines are the respective theoretical approximations to the simulations (details given in section III). Parameters: $N_P = 1000$, $D_R = 0.1$ s^{-1}, $v = 20$ μm s^{-1}, $d = 60$ μm, unless otherwise stated.

We derive the diffusion coefficient from N_P simulated particle tracks by fitting the mean square displacement as $\langle \delta x(t)^2 \rangle = 4D_{\rm eff}t + 4D_{\rm eff}\eta[\exp(-t/\eta) - 1]$ (a result easily derived for self-propelled particles using a standard method, see for example [42]), where the time scale of ballistic motion, η, is the second fitting parameter.

We first establish the diffusive properties of active particles with a reflective boundary condition. Here, we recognize an analogy to the Lorentz gas model, in which particles move ballistically between obstacles [35]. The Santalo formula is a well-known result for the mean-free path of a Lorentz gas [43] given by $\lambda = \pi A/P$, where A and P are the free area and obstacle perimeter in a unit cell (shown for a hexagonal lattice in Fig. 2(a)), respectively. Since the active particles move diffusively at large time scales, we derive an active version of Santalo's formula with a circle of radius l_p as an additional boundary, as in Fig. 2(b). This yields the mean-free path of an active particle as $\tilde{\lambda}_{l_p} = \pi N A/(NP + 2\pi l_p)$, where N is the number of unit cells included in the circle of radius l_p. For a hexagonal lattice of circular obstacles, we obtain $A = \sqrt{3}d^2/2 - \pi R^2$, $P = 2\pi R$ and $N = \pi l_p^2/(\sqrt{3}d^2/2)$. Note that in order to obtain the fit in Fig. 3(a), we find that this mean free path has to be scaled by $\pi/2$, i.e. $\lambda_{lp} = 2\tilde{\lambda}_{lp}/\pi$. We believe that this is due to the choice of averaging conditions made in earlier work [43]. As shown in Fig. 3(a), applying this adjusted mean-free path in $D = \lambda_{l_p} v/2$ matches the simulations. The inset plots the theoretical prediction and the diffusion coefficient fitted from simulations on a lin-log scale, showing that at large R/d the diffusion coefficient scales as $\ln(1/\rho)$, where obstacle density $\rho = 2\pi/\sqrt{3}\,(R/d)^2$. If we vary the obstacle separation d instead of the obstacle radius R, we see, as expected, that the diffusion coefficient approaches D_0 when $d \gg l_p$ (results not shown). We can understand the reduction in diffusion coefficient qualitatively: as the obstacle density increases, particles spend most of their time in the wells between triplets of obstacles in the hexagonal lattice, and their motion becomes a jump-diffusion process from well to well, as described by Machta and Zwanzig [35] and illustrated by the particle track in Fig. 1(c).

The slide-off boundary condition preserves the particle orientation $\mathbf{p}$ at the point of collision. Here, we consider two different cases: i) when rotational diffusion is fully suppressed while on the obstacle, here called the deterministic slide-off condition, and ii) when rotational diffusion remains the same as in free space while on the obstacle, here called the stochastic slide-off condition. In both cases, the diffusion coefficient $D_{\rm SO}$ is equal to the free diffusion coefficient D_0 in the limit of small (or very separated) obstacles, as shown in Fig. 3(b). However, at higher obstacle densities, the deterministic slide-off diffusion coefficient increases significantly over the free space case (see the purple markers in Fig. 3(b)). This increase appears despite the decrease in speed on the obstacle. As the speed on the obstacle is given by $v = v_0 \cos\beta$, the particle will propagate very slowly when it is oriented at right angles to the surface. Restoring rotational diffusion on the obstacle surface dramatically changes the dependence of $D_{\rm SO}$ on the obstacle density. The stochastic slide-off diffusion coefficient decreases monotonically,

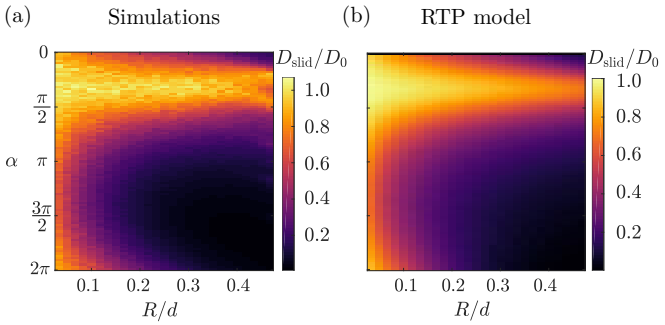

FIG. 4. Diffusion with sliding boundary condition. (a) Simulations reveal dependence on both obstacle density and central angle. (b) Theoretical prediction Eq. (3) with $\tau_c = \lambda/v$ in $\tau = \tau_c + \tau_R$ and $\langle\cos\psi\rangle$ given by Eq. (6). Parameters: $N_P = 1000$, $D_R = 0.1\ \mathrm{s}^{-1}$, $v = 20\ \mu\mathrm{m\,s}^{-1}$, $d = 60\ \mu$m.

but this is still much higher than the Lorentz gas result (compare the green markers in Fig. 3(b) to the markers in Fig. 3(a)). If the rotational diffusion is increased both in free space and on the obstacle, the effect of the obstacle lattice on the relative diffusion is reduced (green vs. orange markers in Fig. 3(b)).

Numerical solutions of Eqs. (1) and (2) with a sliding boundary condition reveal that diffusion depends both on the obstacle density ρ and the central angle α [see Fig. 4(a)]. A large diffusive transport can be sustained even at large obstacle density ρ for certain values of α. Despite frequent obstacle collisions, the reorientation is small because the sliding boundary condition conserves the major component of the velocity vector for small to intermediate values of α. Large values of α, on the other hand, cause a particle to retrace much of its track. The typical pusher surface interaction can, thus, lead to an increase in effective diffusion compared to the classical reflection.

III. RUN-AND-TUMBLE FRAMEWORK

While the active Santalo formula matches the reflective simulations well in Fig. 3(a), it cannot account for the persistence introduced by the sliding and slide-off boundary conditions, and a different approach is required. We derive a theoretical description based on the model of run-and-tumble particles (RTP) [44, 45]. Here an effective 'tumble' means an obstacle-induced reorientation of the particle, and the 'run' between obstacle collisions is influenced by rotational diffusion. The diffusion coefficient for an RTP also undergoing rotational diffusion is known to be

$$D = \frac{v^2}{2[D_R + (1 - \langle\cos\psi\rangle)/\tau]}, \tag{3}$$

where τ is the mean run time and $\psi = \psi(\alpha, P(\beta))$ is the reorientation angle during a tumble [46, 47]. In the following, we will derive expressions for the parameters in Eq. (3): i) the reorientation function $\langle\cos\psi\rangle$, ii) the mean run time τ, and iii) the effective speed v based on the microscopic details of the sliding, the reflecting and the slide-off boundary conditions. We will then apply the RTP model with those parameters to the simulations presented in the previous section.

Reorientation function

The reorientation angle is the combination of alignment upon collision with the obstacle, β, and sliding according to the central angle, α: $\psi = \alpha - \beta$ (see Appendix B for derivation). The average $\langle\cos\psi\rangle$ is performed over the collision angle β, with probability distribution $P(\beta)$.

To derive the distribution, we consider a single circular obstacle of radius R. A particle can start at any distance x from the centre of the obstacle, with its initial direction ϕ uniformly distributed (see Appendix A for schematic). The particle moves in a straight line, and may or may not collide with the obstacle. We ask: given a uniform distribution of starting directions, what is the observed collision angle distribution $P(\beta)$?

For this, we need only consider a truncated distribution $P(\phi) = 1/(2\cos^{-1}(R/x))$ between the angles $-\cos^{-1}(R/x) \le \phi \le \cos^{-1}(R/x)$, where the particle will only graze the obstacle at a tangent to its surface. Beyond this range of angles, the particle will not hit the obstacle. From the sine rule, we can see quickly that

$$\frac{x}{\sin(\pi/2 + \beta)} = \frac{R}{\sin\phi}, \tag{4}$$

and so $\phi(\beta, x) = \sin^{-1}\left(\frac{R}{x}\cos\beta\right)$. The transformation between the uniform initial angle distribution $P(\phi)$ and the collision angle distribution $P_x(\beta)$ is given by $P_x(\beta) = P(\phi)|d\phi/d\beta|$, where $|d\phi/d\beta| = R\sin(\beta)(x\sqrt{1 - (R^2\cos^2\beta)/x^2})^{-1}$ is the Jacobian of the transformation. We can write the collision angle distribution averaged over all space as

$$P(\beta) = \frac{\int_R^L dx\ 2\pi x\ P_x(\beta)}{\int_0^\pi d\beta \int_R^L dx\ 2\pi x\ P_x(\beta)} = \frac{\sin\beta}{2}, \tag{5}$$

where L is the system size. Here, the factors of $2\pi x$ arise from summing over annular regions of starting points. The denominator is a normalisation factor. Despite using deterministic trajectories to calculate this distribution, it fits the observed collision angle distribution for simulations at low densities. Performing the average gives the reorientation function as:

$$\begin{aligned}\langle\cos\psi\rangle &= 2\int_0^{\pi/2} \cos(\alpha - \beta)P(\beta)d\beta \\ &= \frac{1}{4}(2\cos\alpha + \pi\sin\alpha),\end{aligned} \tag{6}$$

noting that $\cos\psi$ is even about $\beta = \pi/2$. This framework is general, and so can be adapted for specific boundary conditions, as long as the reorientation function $\langle\cos\psi\rangle$ can be determined. For the reflecting boundary condition, $\psi = 2\beta$, and $\langle\cos\psi\rangle = -1/3$. For the deterministic slide-off condition, there is by definition no reorientation, and so $\langle\cos\psi\rangle = 1$. For the stochastic slide-off condition, however, the particle can deviate in its orientation while on the obstacle, and so the reorientation function $\langle\cos\psi\rangle \leq 1$. For this condition, the reorientation function depends on the obstacle radius compared to the persistence length, $R/l_p = RD_R/v$. This parameter gives an idea of whether diffusion (D_R) or movement around the pillar (v/R) has a larger effect on the particle's orientation. To see this, consider an extremely large obstacle (large R/l_p). Then, change in the particle's surface angle due to movement around the obstacle will be very small, as the curvature is low. Therefore, diffusion will dominate the reorientation, and $\langle\cos\psi\rangle < 1$. Conversely, a small obstacle will not allow much time for reorientation due to rotational diffusion before the particle leaves again. Modelling reorientation for the stochastic slide-off condition is challenging, and it is not possible to find an exact expression, but numerical solutions show that a very good approximation for small to medium R/l_p (for details, see Appendix C 1) is given by $\langle\cos\psi\rangle \approx 1 - \frac{1}{2}\sqrt{R/l_p}$.

Residence time

The second parameter in the RTP model (3) is the mean run time τ, which corresponds to the time between obstacle collisions. Because the characteristic time between collisions is independent of the details of the random walk and depends purely on confinement [48], we use the mean collision time $\tau_c = \lambda/v$ for all boundary conditions, where λ is the mean free path given by Santalo's formula. For the sliding boundary condition, the mean run time is adjusted by the time spent on an obstacle, i.e. $\tau = \tau_c + \tau_R$, with residence time $\tau_R = R\alpha/v$. For the deterministic slide-off condition $\tau_R = \pi R/2v$ (for details see Appendix C 2). Note that this is not equal to $R\hat{\alpha}/v$, because v is reduced on the obstacle, and so $\tau_R > R\hat{\alpha}/v$. The addition of rotational diffusion also changes the residence time. For the stochastic slide-off condition we must solve a complicated mean first passage time problem (again, for details see Appendix C 2). Nevertheless, it turns out that a very reasonable fit to numerical solutions of the residence time is given by:

$$\tau_R = \frac{\pi R}{2v}\frac{1}{1 + \pi R/2l_p}. \tag{7}$$

This expression gives the deterministic time $\tau_R \to \pi R/2v$ at low rotational diffusion (small R/l_p), and the expected time to exit the free space interval $\{0, \pi\}$ for large rotational diffusion (large R/l_p): $\tau_R \to 1/D_R$. This latter time assumes that we can neglect the contribution from deterministic drift at large enough rotational diffusion values.

Effective speed

A final consideration is that travelling on the obstacle causes an effective reduction in velocity. When the particle traces along the pillar, it travels a distance $l < v\tau_R$, which gives $v_{\text{obs}} = l/\tau_R$. By the cosine rule, $l = R\sqrt{2 - 2\cos\alpha}$ for the sliding boundary condition. It follows that $l = R\sqrt{2 - 2\cos(1)}$ for the deterministic slide-off condition. For the stochastic slide-off condition, we require the average reorientation angle $\hat{\alpha}$. This is solved by averaging over the initial angle distribution (for details on $\hat{\alpha}$, see Appendix C 1):

$$\hat{\alpha} = \int_0^\beta d\beta\, \hat{\alpha}(\beta)\sin\beta. \tag{8}$$

Again, this can be solved numerically, and we find a good approximation to $\hat{\alpha}$ for small to medium R/l_p (see Appendix C 3) is:

$$\hat{\alpha} \approx 1 - \sqrt{\frac{\pi R}{2l_p}} + \left(\frac{R}{2l_p}\right)^{3/2}, \tag{9}$$

and then, the average distance travelled for the stochastic slide-off condition is $l = R\sqrt{1 - \cos\hat{\alpha}}$. Using those distances travelled, the effective speed in Eq. (3) is then $v_{\text{eff}} = v\tau_c/\tau + v_{\text{obs}}\tau_R/\tau = v\tau_c/\tau + l/\tau$.

Comparison with simulation

We first apply the RTP theory to simulations with reflecting boundary condition, using $\langle\cos\psi\rangle = -1/3$ and $\tau_R = 0$. As shown in Fig. 3(a), the RTP model with $\tau = \tau_c$ yields a good approximation of the simulation results. As a comparison, the RTP model with a recently derived mean collision time [31], where $\tau_c^B = 1/\rho$, approximates the simulations at low densities but diverges in the high density regime.

For the deterministic slide-off condition, we observed an increase in diffusion coefficient compared to the free diffusion in Fig. 3(b). We suspect the supression of rotational diffusion as cause for this increase, and, thus, use an effective rotational diffusion $D_R^{\text{eff}} = D_R\tau_c/\tau$ in Eq.(3). With this correction, the RTP model is a good approximation of the simulation results, see dashed purple line. For the stochastic slide-off condition, the RTP model in Fig. 3(b) reproduces the trends seen in the simulation results: we see a reduction in the diffusion coefficient as the obstacle density increases. The relative decrease in the diffusion coefficient to that of free space is smaller as the persistence length decreases: if the particle is more prone to reorientation in free space, the effect of reorientation due to the obstacles is smaller, as can be seen by comparing the green and orange dashed curves in Fig. 3(b).

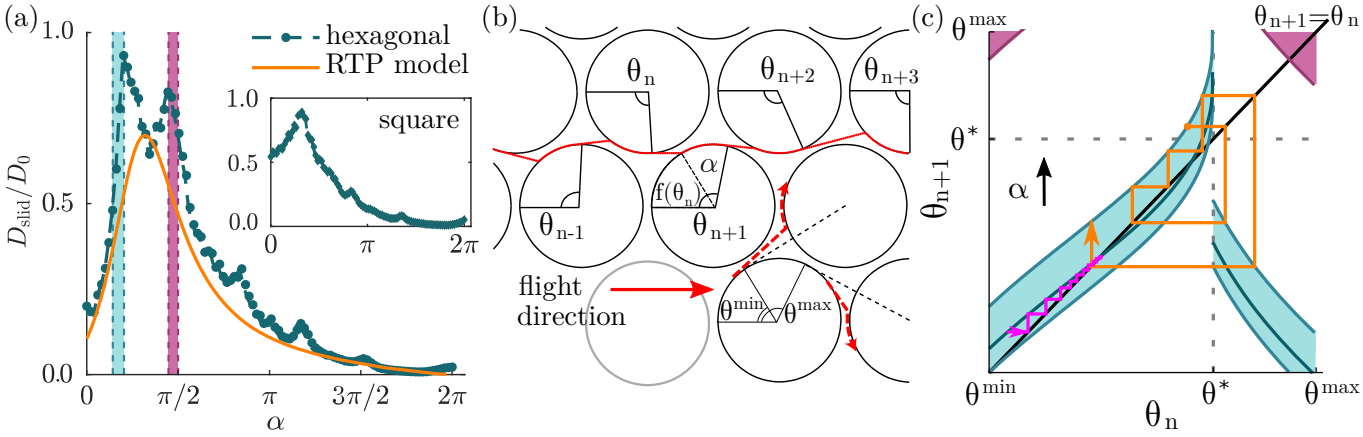

FIG. 5. Geometric effects for sliding BC. (a) The discrepancy between the RTP model and the hexagonal lattice simulation results at high density ($R/d = 0.47$) is centred around the deterministic stable regions [shaded as in (c)], revealing influence of geometry. Inset: Diffusion coefficient for a square lattice. (b) Schematic of a 1-D system, considering a flight along one channel in the lattice. The leaving angle at each pillar is given by θ_n. The lower schematic shows possible termination of flights in a horizontal channel. (c) Iterative map of the leaving angle as a function of the previous leaving angle for different central angles α, $\theta_{n+1} = f(\theta_n) + \alpha$. The shaded regions correspond to regions of stable flights. Stable fixed points cross the dashed $\theta_{n+1} = \theta_n$ line with a gradient between -1 and 1 (a mapping with a stable fixed point is shown in the lower shaded region, with an example trajectory in pink). An example of a bounded mapping of leaving angles is shown as orange trajectory.

However, the RTP model predicts a much sharper decline in the diffusion coefficient at larger values of R. This is the first hint that the obstacle lattice may be playing a large role at high densities.

For the sliding boundary condition, the RTP framework reproduces the main features of the simulations, see Figs. 4(a) and 4(b): it maintains a large diffusion coefficient for small to intermediate α. Since τ_c is independent of the boundary condition, this must stem from the reorientation function $\langle \cos\psi \rangle$ in Eq. (6), which has a maximum at $\alpha \approx \pi/3$ and a minimum at $\alpha \approx 4\pi/3$. These extrema coincide with the predicted maximum and minimum of the diffusion coefficient observed for small to intermediate R/d in Fig. 4(b). Beyond $\alpha = 4\pi/3$, any increase in the diffusion coefficient due to the reorientation function is suppressed by the increase in residence time τ_R at large R and α. Note that, since the RTP model is oblivious to obstacle arrangement, these results also apply to random lattices at low densities.

IV. HIGH-DENSITY GEOMETRICAL EFFECTS

While the RTP model accounts for the diffusion coefficient $D_{\rm slid}$ of the sliding boundary condition at low to intermediate obstacle densities, it fails to completely describe the simulations at high density. Figure 5(a) shows fixed $R/d = 0.47$ (the largest value) cross-sections of the surfaces in Figures 4(a) and 4(b). At this high density, the diffusion coefficient for the hexagonal lattice simulations has peaks that exceed the RTP model. There are two of these peaks at low α as well as smaller overshoots at higher α. However, if we instead perform the simulations in a square lattice, we get a different peak structure, with a single peak at low α. We will show that this is due to the geometry of the lattice, and its guiding effect on the self-propelled particles.

For the geometry of the lattice to influence the particle paths, there must be a correlation between successive collisions with pillars. This means that the particle must not lose the memory of its orientation between collisions, i.e. the obstacle separation must be much smaller than the persistence length, $d - 2R \ll l_p$. In this case, a purely deterministic model ($D_R = 0$) provides a good approximation to explore correlations between collisions. In such a model, the particle travels in a straight line between pillars, and is reoriented by α by sliding scattering. We consider a 'channel' defined by two rows of pillars within the lattice (Fig. 5(b)). A particle traverses the channel by skirting around pillars, leaving the surface of the nth pillar with a polar angle θ_n. For deterministic (ballistic) dynamics between collisions, we can completely specify a trajectory by the 'flight' $\{\theta_n\}_{n=1}^{N}$, the sequence of leaving angles from successive collisions, as in Fig. 5(b). The sequence size N defines the flight length. Successive leaving angles are determined by the recurrence relation: $\theta_{n+1} = g_\alpha(\theta_n) = f(\theta_n) + \alpha$, where, in this deterministic model, $f(\theta_n)$ is a function determined solely by the geometry (see Appendix D for the functional form).

As the particle moves along a channel during a flight, it can transition between pillars on the opposite (e.g. $\theta_{n-1} \to \theta_n$) or same (e.g. $\theta_{n+2} \to \theta_{n+3}$) side of the channel, as shown in Fig. 5(b). For $R/d > \sqrt{3}/4$ (the close-packed limit of overlapping pillars), a critical angle $\theta_n = \theta^*$ emerges that determines on which side of the channel a particle will next hit. If $\theta_n \le \theta^*$, the particle will cross over to an obstacle on the other side of the

channel, while if $\theta_n > \theta^*$, it will move to one on the same side. This means the map $g_\alpha(\theta_n)$ is discontinuous at $\theta_n = \theta^*$, as in Fig. 5(c).

The flights considered in the deterministic model correspond well to what we observe in our simulations. At high densities, these show particle trajectories made up of long flights along lattice channels, interrupted by 'tumbles' into the next long flight. The deterministic model allows to establish if the flights are geometrical in origin. In this model, a flight terminates when the leaving angle θ_n becomes too small ($\theta_n < \theta^{\min}$) or too large ($\theta_n > \theta^{\max}$) as it will be deflected out of the channel on its next collision, illustrated in Fig. 5(b). Stable flights are trajectories that remain in the region $\theta^{\min} \leq \theta_n \leq \theta^{\max}$ indefinitely. This can happen in two ways: (i) a stable fixed point may exist (a point θ such that $g_\alpha(\theta) = \theta$, and $|g'_\alpha(\theta)| < 1$), so that long trajectories have a single repeated leaving angle; (ii) the map $g_\alpha(\theta_n)$ is bounded within the allowed region of leaving angles: $\theta^{\min} \leq g_\alpha(\theta_n) \leq \theta^{\max}$ for all $\theta^{\min} \leq \theta_n \leq \theta^{\max}$, so that no trajectory may leave the allowed region. Example trajectories of both types are illustrated in Fig. 5(c).

The iterative map $\theta_{n+1} = g_\alpha(\theta_n)$ is plotted for $R/d = 0.47$ in Fig. 5(c). Two stable ranges (shaded regions) are seen to emerge corresponding to ranges of α, which controls stability. For $\theta_n < \theta^*$, increasing α causes a stable fixed point to develop. Increasing it further, in the range that defines the lower region (shaded in blue), provides a map bounded in the interval $[\theta_{min}, \theta_{max}]$. Flights in this lower shaded region bounce from one side of the channel to the other. If α is increased further, the map again becomes unbounded ($g_\alpha(\theta_n) > \theta^{\max}$) and stability is lost. For $\theta_n > \theta^*$, the upper region (shaded in pink) has a stable fixed point, so that particles perform stable flights by running along only one side of the channel in this region. Stable trajectories from the deterministic model cannot give rise to diffusive behaviour. However, any rotational diffusion, however small, will eventually cause a deviation of trajectory large enough to take the particle out of the stable interval $[\theta^{\min}, \theta^{\max}]$. This will cause flights to terminate, and this is why the observed transport is diffusive, not superdiffusive. In view of the large persistence length of flights for stable values of α, the diffusion coefficient for such flights is expected to be large compared to that corresponding to other values of α. By plotting the stable regions of α predicted by the deterministic model against the simulation results at high density in Fig. 5(a), we see that this is indeed the case: the spikes in diffusion coefficient for the simulations correspond well to the stable regions in the deterministic model. It is important to note that the obstacle sizes we are considering here are below the critical trapping radii tyically found [26, 27]. It is possible to reach a high density state where the obstacle separation is larger than the persistence length, where our results wouldn't hold. However, in this regime, the obstacles would be much larger than the trapping radius, and so particles would be trapped for long periods on obstacles [26, 27], making diffusion very slow. Finally, it is not only in the sliding boundary condition that we see significant deviation from the RTP model. The stochastic slide-off collision rule also exhibits an increase over the bare RTP model as R/d gets very large. Although we do not try to model this here, it is clear from particle trajectories in the simulations (see e.g. Fig. 1(b)) that in this case there is also a geometrical guiding effect (this is also the case for the deterministic slide-off rule).

V. DISCUSSION & CONCLUSIONS

To conclude, we find that non-classical surface interactions significantly impact the active diffusive transport in complex environments, such as ordered obstacle arrays. Compared to a high-density Lorentz gas model, where particles get trapped in the wells of lattices, and the behaviour is jump-diffusive, the sliding and slide-off boundary conditions allow particles to escape these wells and traverse the lattice efficiently. These boundary conditions share certain general features and differences to the classical specular reflection boundary condition. The most striking is that they are not invertible; given an outgoing orientation and leaving point, we cannot infer both the incoming angle and collision point. The sliding condition maps particles with different orientations upon collision to the same leaving point, and so information on the incident angle is lost. Similarly, the deterministic slide-off condition maps particles with the same incident angles but different collision points onto the same leaving point. The stochastic slide-off condition loses both pieces of information. We believe this non-invertibility provides a stabilising effect on trajectories due to geometrical guiding at high obstacle densities.

Our results highlight the importance of choosing realistic microscopic boundary conditions to obtain realistic macroscopic dynamics. In particular, models employing reflective boundary conditions, e.g. those used in [40, 41] to describe bacteria in porous media, should not give realistic results for active particles. While this is generally obvious considering detailed balance [5], the theoretical framework we have developed allows the formulation of particular predictions to be tested experimentally, for instance, using bacteria in microfluidic arrays. In particular, it would be interesting to test our prediction of large diffusive transport in dense arrays. The RTP model presented here is general in the sense that it can be applied for different lattices and particles. A different lattice of obstacles requires the re-calculation of $\langle \cos\psi \rangle$ and τ_c. A change in the scattering interaction, on the other hand, requires specification of $\langle \cos\psi \rangle$, τ_R, and potentially v_{obs}, e.g. using experimental measurements. While the description was developed for lattices, we note that, when the number of obstacle contacts is low, our results hold for random environments too.

Finally, since the time bacteria spend on an obstacle is a function of its curvature and the force dipole strength of the bacterium [26, 27], it is interesting to consider

the diffusive transport of bacterial species with different dipole strengths. The latter depend on body shape and propulsion mechanism, which vary between species. It would be interesting to investigate if certain species, e.g. soil bacteria, have hydrodynamic properties tailored towards guided transport in complex environments[34]. This could be achieved combining our theoretical framework and microfluidic experiments.

ACKNOWLEDGMENTS

We thank Eugene Terentjev, Mark Warner and Mike Cates for helpful discussions and feedback on the manuscript. This work has been funded by EPSRC EP/M508007/1 (S.B.), EP/L504920/1 and EP/N509620/1 (T.J.), and the Winton Programme for the Physics of Sustainability (T.J., O.C.).

[1] C. Bechinger, R. Di Leonardo, H. Löwen, C. Reichhardt, G. Volpe, and G. Volpe, Rev. Mod. Phys. **88**, 045006 (2016).
[2] J. G. Puckett, R. Ni, and N. T. Ouellette, Phys. Rev. Lett. **114**, 258103 (2015).
[3] M. Sinhuber and N. T. Ouellette, Phys. Rev. Lett. **119**, 178003 (2017).
[4] F. Giavazzi, M. Paoluzzi, M. Macchi, D. Bi, G. Scita, M. L. Manning, R. Cerbino, and M. C. Marchetti, Soft Matter **14**, 3471 (2018).
[5] M. E. Cates, Rep. Prog. Phys. **75**, 042601 (2012).
[6] T. Sanchez, D. T. Chen, S. J. DeCamp, M. Heymann, and Z. Dogic, Nature **491**, 431 (2012).
[7] F. C. Keber, E. Loiseau, T. Sanchez, S. J. DeCamp, L. Giomi, M. J. Bowick, M. C. Marchetti, Z. Dogic, and A. R. Bausch, Science **345**, 1135 (2014).
[8] A.-Y. Jee, S. Dutta, Y.-K. Cho, T. Tlusty, and S. Granick, Proc. Natl. Acad. Sci. USA **115**, 14 (2018).
[9] J. W. Costerton, P. S. Stewart, and E. P. Greenberg, Science **284**, 1318 (1999).
[10] K. Drescher, J. Dunkel, L. H. Cisneros, S. Ganguly, and R. E. Goldstein, Proc. Natl. Acad. Sci. USA **108**, 10940 (2011).
[11] N. Heddergott, T. Krüger, S. B. Babu, A. Wei, E. Stellamanns, S. Uppaluri, T. Pfohl, H. Stark, and M. Engstler, PLoS Pathog. **8**, e1003023 (2012).
[12] M. Eisenbach and L. C. Giojalas, Nat. Rev. Mol. Cell Biol. **7**, 276 (2006).
[13] A. Guidobaldi, Y. Jeyaram, I. Berdakin, V. V. Moshchalkov, C. A. Condat, V. I. Marconi, L. Giojalas, and A. V. Silhanek, Phys. Rev. E **89**, 032720 (2014).
[14] P. Denissenko, V. Kantsler, D. J. Smith, and J. Kirkman-Brown, Proc. Natl. Acad. Sci. USA **109**, 8007 (2012).
[15] J. Simmchen, J. Katuri, W. E. Uspal, M. N. Popescu, M. Tasinkevych, and S. Sánchez, Nat. Comms. **7**, 10598 (2016).
[16] G. Volpe, I. Buttinoni, D. Vogt, H.-J. Kümmerer, and C. Bechinger, Soft Matter **7**, 8810 (2011).
[17] A. T. Brown, I. D. Vladescu, A. Dawson, T. Vissers, J. Schwarz-Linek, J. S. Lintuvuori, and W. C. K. Poon, Soft Matter **12**, 131 (2016).
[18] M. S. D. Wykes, X. Zhong, J. Tong, T. Adachi, Y. Liu, L. Ristroph, M. D. Ward, M. J. Shelley, and J. Zhang, Soft Matter **13**, 4681 (2017).
[19] V. Kantsler, J. Dunkel, M. Polin, and R. E. Goldstein, Proc. Natl. Acad. Sci. USA **110**, 1187 (2013).
[20] M. Contino, E. Lushi, I. Tuval, V. Kantsler, and M. Polin, Phys. Rev. Lett. **115**, 258102 (2015).
[21] E. Lushi, V. Kantsler, and R. E. Goldstein, Phys. Rev. E **96**, 023102 (2017).
[22] S. E. Spagnolie, C. Wahl, J. Lukasik, and J.-L. Thiffeault, Physica D **341**, 33 (2017).
[23] A. P. Berke, L. Turner, H. C. Berg, and E. Lauga, Phys. Rev. Lett. **101**, 038102 (2008).
[24] G. Li and J. X. Tang, Phys. Rev. Lett. **103**, 078101 (2009).
[25] J. Elgeti, U. B. Kaupp, and G. Gompper, Biophys. J. **99**, 1018 (2010).
[26] O. Sipos, K. Nagy, R. Di Leonardo, and P. Galajda, Phys. Rev. Lett. **114**, 258104 (2015).
[27] S. E. Spagnolie, G. R. Moreno-Flores, D. Bartolo, and E. Lauga, Soft Matter **11**, 3396 (2015).
[28] J. Elgeti, R. G. Winkler, and G. Gompper, Rep. Prog. Phys. **78**, 056601 (2015).
[29] A. Chamolly, T. Ishikawa, and E. Lauga, New J. Phys. **19**, 115001 (2017).
[30] O. Chepizhko and F. Peruani, Phys. Rev. Lett. **111**, 160604 (2013).
[31] T. Bertrand, Y. Zhao, O. Bénichou, J. Tailleur, and R. Voituriez, Phys. Rev. Lett. **120**, 198103 (2018).
[32] M. Zeitz, K. Wolff, and H. Stark, Eur. Phys. J. E **40**, 23 (2017).
[33] S. Thutupalli, D. Geyer, R. Singh, R. Adhikari, and H. A. Stone, Proc. Natl. Acad. Sci. USA **115**, 5403 (2018).
[34] M. Raatz, M. Hintsche, M. Bahrs, M. Theves, and C. Beta, Eur. Phys. J. Spec. Top. **224**, 1185 (2015).
[35] J. Machta and R. Zwanzig, Phys. Rev. Lett. **50**, 1959 (1983).
[36] H. C. Berg, *Random walks in biology* (Princeton University Press, 1993).
[37] S. Tavaddod, M. Charsooghi, F. Abdi, H. Khalesifard, and R. Golestanian, Eur. Phys. J. E **34**, 16 (2011).
[38] S. Das, A. Garg, A. I. Campbell, J. Howse, A. Sen, D. Velegol, R. Golestanian, and S. J. Ebbens, Nat. Commun. **6**, 8999 (2015).
[39] C. Reichhardt and C. O. Reichhardt, Phys. Rev. E **97**, 052613 (2018).

[40] J. W. Barton and R. M. Ford, Biotechnol. Bioeng. **53**, 487 (1997).
[41] R. M. Ford and R. W. Harvey, Adv Water Resour **30**, 1608 (2007).
[42] H. Risken, *The Fokker-Planck equation: methods of solution and applications* (Springer, 1984).
[43] N. Chernov, J. Stat. Phys. **88**, 1 (1997).
[44] J. Tailleur and M. E. Cates, Phys. Rev. Lett. **100**, 218103 (2008).
[45] M. J. Schnitzer, Phys. Rev. E **48**, 2553 (1993).
[46] J. Taktikos, H. Stark, and V. Zaburdaev, PloS One **8**, e81936 (2013).
[47] P. S. Lovely and F. W. Dahlquist, J. Theor. Biol. **50**, 477 (1975).
[48] S. Blanco and R. Fournier, EPL **61**, 168 (2003).
[49] A. Szabo, K. Schulten, and Z. Schulten, J. Chem. Phys. **72**, 4350 (1980).

Appendix A: Collision angle distribution

Figure 6 shows the geometry considered when we ask for the collision angle distribution $P(\beta)$. We consider a single point in space, and then average over all space using circular shells (giving the factors of $2\pi x$ in the integrals in Eq. (5)).

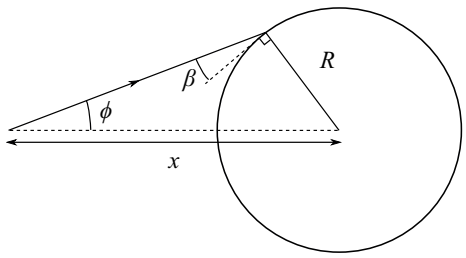

FIG. 6. Schematic of the set-up to determine the incoming angle distribution. A particle starts a distance x from the centre of the pillar, and then travels at an orientation ϕ relative to the line joining the centre of the circle to the particle's origin, hitting the circle at an angle β to the tangent of the circle.

Appendix B: Reorientation function - sliding condition

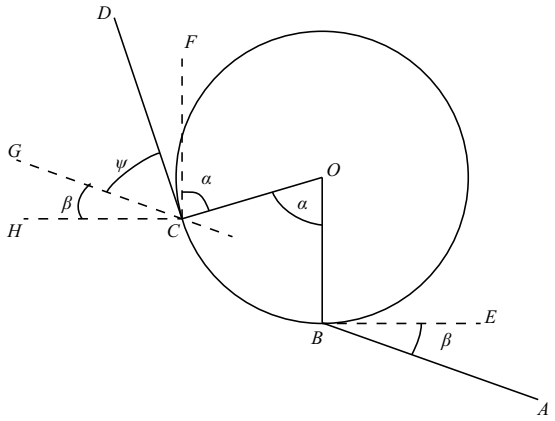

FIG. 7. Schematic of the reorientation angle θ as a function of α and β. The sliding particle travels along the path ABCD. Lines OB and CF are parallel, as are lines AB and CG, and lines EB and CH.

By construction (see Fig. 7), angle FCH must be a right angle. Since the particle leaves at a tangent, OCD is also a right angle. By the alternate angle theorem, OCF=α, and so DCF=$\pi/2-\alpha$. Therefore, $\psi = \pi/2 - \beta - (\pi/2 - \alpha) = \alpha - \beta$.

Appendix C: Slide-off boundary condition: RTP parameter derivations

1. Reorientation function

To model the dependence of the reorientation function for the stochastic slide-off condition, we must look at the underlying Langevin equation of the angle the particle makes with the obstacle surface, Θ:

$$\dot{\Theta} = -\frac{v}{R}\cos\Theta + \sqrt{2D_R}\xi(t). \tag{C1}$$

The deterministic drift comes from movement around the surface of the pillar. We want to know the average distance traversed around the pillar for a given incident angle, $\hat{\alpha}(\beta)$. We find this by adding up all the contributions of the particle's movement over the surface during its interaction with the pillar:

$$\hat{\alpha}(\beta) = \left\langle \int_0^T dt\ \frac{v}{R}\cos\Theta(t) \right\rangle_{\Theta(0)=\beta}, \tag{C2}$$

where T is the time at which the particle angle Θ first reaches 0 or π and leaves the obstacle. We can substitute

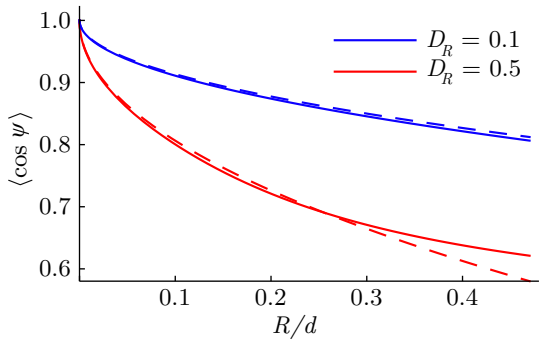

FIG. 8. Numerical solution for the reorientation function in Eq. (C4) (thick curves) vs. the analytical approximation (dashed curves) in Eq. (C5) for $D_R = 0.1\text{s}^{-1}$ (blue curves) and $D_R = 0.5\text{s}^{-1}$ (red curves). Other simulation parameters as in the main text.

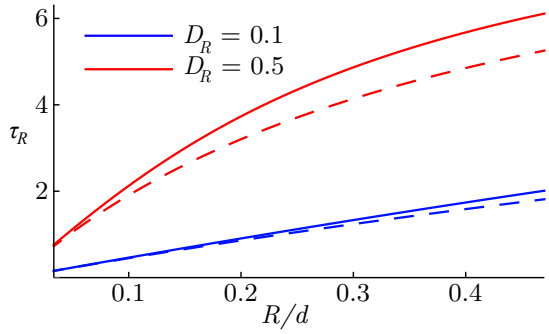

FIG. 9. Numerical solution of Eq. (C7) (thick curves) compared to the analytical approximation in Eq. (C9) (dashed curves). These are plotted for $D_R = 0.1\text{s}^{-1}$ (blue curves) and $D_R = 0.5\text{s}^{-1}$ (red curves). Other simulation parameters as in the main text.

using the Langevin equation (C1):

$$\begin{aligned}\hat{\alpha}(\beta) &= \left\langle \int_0^T dt\ \left(-\dot{\Theta} + \sqrt{2D_R}\xi(t)\right)\right\rangle_{\Theta(0)=\beta} \\ &= \beta - \langle\Theta(T)\rangle_{\Theta(0)=\beta}.\end{aligned} \tag{C3}$$

Here we have made the assumption that the stochastic integral vanishes, which is not obviously true, as we are not averaging over all trajectories at the time T, only those ones that reach the boundaries for the first time. However, this seems reasonable, given we may exit the region on both sides. To get the reorientation, we integrate over the incident angle:

$$\begin{aligned}\langle\cos\psi\rangle &= 2\int_0^{\pi/2} \cos(\hat{\alpha}(\beta) - \beta)P(\beta)d\beta \\ &= \int_0^{\pi/2} d\beta\ \sin\beta\cos\langle\Theta(T)\rangle_{x(0)=\beta}.\end{aligned} \tag{C4}$$

This expression can be evaluated numerically, and a very good approximation for small to medium R/l_p (see Fig. 8) is given by:

$$\langle\cos\psi\rangle \approx 1 - \frac{1}{2}\sqrt{\frac{R}{l_p}}. \tag{C5}$$

2. Residence time

To get the residence time for the deterministic slide-off condition, we must take into account speed reduction on the obstacle. Accordingly, we may write the residence time as an integral:

$$\begin{aligned}\tau_R(\beta) &= \int_\beta^0 \frac{Rd\Theta}{v\cos\Theta} \\ &= \frac{R}{v}\ln\left[1 + \frac{2}{\cos(\beta/2) - 1}\right]\end{aligned} \tag{C6}$$

The residence time averaged over the incident angle distribution is then

$$\tau_R = \int_0^{\pi/2} d\beta\ \tau_R(\beta)\sin\beta = \frac{\pi R}{2v}. \tag{C7}$$

Addition of rotational diffusion on the obstacles makes analysis more difficult. Now, the residence time can be characterised by the mean hitting time of the Langevin equation (C1) on the exiting boundaries. This has a known expression [49]:

$$\tau_R(\beta) = \frac{1}{D_R}\int_0^\beta dy\ e^{l_p\sin y/R}\int_y^{\pi/2} d\Theta\ e^{-l_p\sin\Theta/R}, \tag{C8}$$

where we assumed a reflecting boundary at $\Theta = \pi/2$ and an absorbing boundary at $\Theta = 0$. Again, it is possible to make headway by asymptotics on this integral, but it turns out a more intuitive approximation suffices. For small rotational diffusion $l_p \gg R$, we find that drift time $\tau_{\text{drift}} = \pi R/2v$ dominates the mean first passage time. However, for large rotational diffusion $l_p \ll R$, we may expect that diffusion time, $\tau_{\text{diff}} = 1/D_R$ – calculated as the mean first passage time out of a flat potential for the incident angle distribution $P(\beta)$ – dominates. It turns out that a very reasonable fit to numerical solutions of the integral is

$$\tau_R = \frac{\tau_{\text{drift}}\tau_{\text{diff}}}{\tau_{\text{drift}} + \tau_{\text{diff}}} = \frac{\pi R}{2v}\frac{1}{1 + \pi R/2l_p}, \tag{C9}$$

see Fig. C 2.

3. Effective speed

To find the effective speed we have to find the average angle travelled over the pillar, $\hat{\alpha}$. Using that

$$\hat{\alpha} = \int_0^{\pi/2} d\beta\ \hat{\alpha}(\beta)\sin\beta, \tag{C10}$$

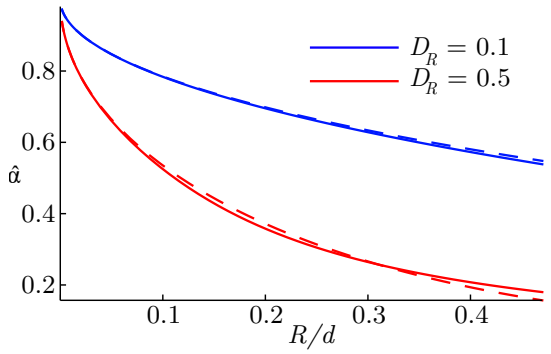

FIG. 10. Numerical solution of $\hat{\alpha}$ (thick curves) vs. the analytical approximation in Eq. (C11) (dashed curves), for $D_R = 0.1\text{s}^{-1}$ (blue curves) and $D_R = 0.5\text{s}^{-1}$ (red curves). Other simulation parameters as in the main text.

and the definition of $\hat{\alpha}(\beta)$ in Eq. (C3), we can find $\hat{\alpha}$ numerically. It turns out the numerical solution is very close to an analytical approximation:

$$\hat{\alpha} \approx 1 - \sqrt{\frac{\pi R}{2l_p}} + \left(\frac{R}{2l_p}\right)^{3/2}, \tag{C11}$$

as shown in Fig. 10.

Appendix D: Geometrical guiding effect

When the radius $R > \sqrt{3}d/4$, the lattice has a nearest neighbour horizon; any straight line drawn from the surface of a pillar must hit one of its nearest neighbours. In this case, for the sliding boundary condition, in a simplified lattice of two rows, we can find the sequence of leaving angles from pillars along a run, as detailed in the main text. The function $f(\theta_n)$ can be determined through geometry, and takes the form

$$f(\theta_n) = \begin{cases} \cos^{-1}\left(1 + \dfrac{d}{R}\sin\left(\dfrac{\pi}{6} - \theta_n\right)\right) - \theta_n, & \theta_n < \theta^* \\ \theta_n - \cos^{-1}\left(1 + \dfrac{d}{R}\cos\theta_n\right), & \theta_n \geq \theta^* \end{cases} \tag{D1}$$

The angle $\theta^* = 2\pi/3 - \cos^{-1}(R/d)$ is a transition angle. For $\theta_n < \theta^*$, the particle will hit a pillar on the opposite side of the channel, and for $\theta \geq \theta^*$ the particle will hit on the same side of the channel.